Mechanotransduction-on-Chip: Vessel-Chip Model of Endothelial YAP Mechanobiology Reveals Matrix Stiffness Impedes Shear Mechanoresponse

Journal:	*Lab on a Chip*
Manuscript ID	LC-ART-12-2020-001283.R1
Article Type:	Paper
Date Submitted by the Author:	10-Mar-2021
Complete List of Authors:	Walther, Brandon; Texas A&M University College Station, Biomedical Engineering; Houston Methodist Research Institute, Cardiovascular Sciences Rajeeva Pandian, Navaneeth Krishna; Texas A&M University College Station, Dept. of Biomedical Engineering Gold, Karli; Texas A&M University College Station, Biomedical Engineering Kiliç, Ecem; Texas A&M University College Station, Biomedical Engineering Sama, Vineeth; Clemson University, Biomedical Engineering Gu, Jianhua; Houston Methodist Research Institute, Department of Nanomedicine Gaharwar, Akhilesh; Texas A&M University College Station, Department of Biomedical Engineering Guiseppi-Elie, Anthony; Texas A&M University College Station, Cooke, John; Houston Methodist Research Institute, Cardiovascular Sciences Jain, Abhishek; Texas A&M University College Station, Biomedical Engineering; Texas A&M University System Health Science Center College of Medicine, Medical Physiology

SCHOLARONE™
Manuscripts

Mechanotransduction-on-Chip: Vessel-Chip Model of Endothelial YAP Mechanobiology

Reveals Matrix Stiffness Impedes Shear Mechanoresponse

Brandon K. Walther[1,2], Navaneeth Krishna Rajeeva Pandian[1], Karli A. Gold[1], Ecem S. Kiliç[1],

Vineeth Sama[3], Jianhua Gu[2], Akhilesh K. Gaharwar[1,4], Anthony Guiseppi-Elie[1,2,5,6], John P.

Cooke[2]*, and Abhishek Jain[1,2,7]*

[1]Department of Biomedical Engineering, Texas A&M University, College Station, Texas 77843, USA
[2]Department of Cardiovascular Sciences, Houston Methodist Institute for Academic Medicine and Houston Methodist Research Institute, 6670 Bertner Ave., Houston, Texas 77030, USA.
[3]Department of Biomedical Engineering, Clemson University, Clemson, South Carolina 29634, USA
[4]Department of Materials Science, Texas A&M University, College Station, Texas 77843, USA
[5]ABTECH Scientific, Inc., Biotechnology Research Park, 800 East Leigh Street, Richmond, Virginia 23219, USA
[6]Department of Biomedical Engineering, Anderson University, Anderson, South Carolina 29621, USA
[7]Department of Medical Physiology, College of Medicine, Texas A&M Health Science Center, Bryan, TX 77807, USA

* Correspondence to Abhishek Jain: a.jain@tamu.edu; John P. Cooke: jpcooke@houstonmethodist.org

Authors, emails, and ORCIDs
Brandon K. Walther; brandonwalther1@tamu.edu (0000-0002-4086-8897)
Navaneeth Krishna Rajeeva Pandian; navnkri@tamu.edu (0000-0003-2623-3630)
Karli A. Gold; kgold@tamu.edu
Ecem Simay Kiliç; ecem_simay@tamu.edu
Vineeth Sama; vsama@g.clemson.edu
Jianhua Gu; jgu@houstonmethodist.org
Akhilesh K. Gaharwar: gaharwar@tamu.edu
Anthony Guiseppi-Elie; aguiseppi@andersonuniversity.edu (0000-0003-3218-9285)
John P. Cooke; jpcooke@houstonmethodist.org (0000-0003-0033-9138)
Abhishek Jain; a.jain@tamu.edu (0000-0003-2235-5139)

Abstract

Endothelial mechanobiology is a key consideration in the progression of vascular dysfunction, including atherosclerosis. However mechanistic connections between the clinically associated physical stimuli, vessel stiffness and shear stress, and how they interact to modulate plaque progression remain incompletely characterized. Vessel-chip systems are excellent candidates for modeling vascular mechanobiology as they may be engineered from the ground up, guided by the mechanical parameters present in human arteries and veins, to recapitulate key features of the vasculature. Here, we report extensive validation of a vessel-chip model of endothelial Yes-associated protein (YAP) mechanobiology, a protein sensitive to both matrix stiffness and shearing forces and, importantly, implicated in atherosclerotic progression. Our model captures the established endothelial mechanoresponse, with endothelial alignment, elongation, reduction of adhesion molecules, and YAP cytoplasmic retention under high laminar shear. Conversely, we observed disturbed morphology, inflammation, and nuclear partitioning under low, high, and high oscillatory shear. Examining targets of YAP transcriptional co-activation, connective tissue growth factor (CTGF) is strongly downregulated by high laminar shear, whereas it is strongly upregulated by low shear or oscillatory flow. Ankyrin repeat domain 1 (ANKRD1) is only upregulated by high oscillatory shear. Verteporfin inhibition of YAP reduced the expression of CTGF but did not affect ANKRD1. Lastly, substrate stiffness modulated the endothelial shear mechanoresponse. Under high shear, softer substrates showed the lowest nuclear localization of YAP whereas stiffer substrates increased nuclear localization. Low shear strongly increased nuclear localization of YAP across stiffnesses. Together, we have validated a model of endothelial mechanobiology and describe a clinically relevant biological connection between matrix stiffness, shear stress, and endothelial activation via YAP mechanobiology.

Introduction

Mechanobiology is a discipline of physiology which focuses on how physical environments and mechanical stimuli influence cell behavior and downstream biochemical responses[1, 2]. Endothelial cells (ECs) form 3-dimensional lumenized structures and respond to physical cues such as varying matrix stiffnesses and fluid shear stresses which play a vital role in modulating endothelial homeostasis, preventing atherosclerotic progression and adverse cardiovascular events[3]. Perturbation of these atheroprotective physical inputs results in EC activation and inflammation. However, flow patterns and magnitudes which induce EC activation (and atherosclerotic progression) are termed disturbed flow[4-6] and contain varying parameters depending on the site occurrence, such as insufficient magnitude (low shear) or stark directional changes (oscillatory or recirculating flow). At sites of disturbed flow, atherosclerotic progression is exacerbated[7].

Matrix stiffening is the other primary physical parameter clinically correlated with adverse cardiovascular events, with sites of arterial stiffening associated strongly with atherosclerosis[8, 9]. Furthermore, computational studies on fluid dynamics in the coronary arteries have associated sites of high wall stiffness and low or disturbed shear as primary predictors of where atherosclerotic plaques developed[10-12]. Together, these correlations indicate that aberrant physical cues from substrate stiffness and shear promote vascular disease. However, the interaction of these vascular parameters in modulating signaling pathways and biological response are difficult to elucidate with current experimental models[13].

Recent work on endothelial mechanobiology has highlighted the *Yorkie* associated homologue

proteins YAP (yes-associated protein) and TAZ (transcriptional coactivator with PDZ-binding

motif; collectively referred to as YAP/TAZ or YAP alone) as mechanosensitive, biological

sensors which are regulated in endothelial cells by mechanical cues like substrate stiffness[14] as

well as shear stresses[15-17]. Extensively studied in the context of cell growth and apoptosis via the

Hippo pathway[18], a variety of biochemical and mechanical cues regulate YAP/TAZ activity[15-24]

apart from Hippo. Unidirectional, high, laminar shear stress; soft substrates; and cell confluence

serve to deactivate YAP activity and cause cytoplasmic retention. Conversely, disturbed flow,

stiff matrices, and lack of cellular confluence serve to activate YAP and induce nuclear

translocation. Importantly, the cell confluence pathways are tied to Hippo signaling, while

substrate stiffness and shear stress (mechanobiology pathways) that affect YAP activity are not[18-21]. Highly relevant to EC YAP mechanobiology and vascular homeostasis is that activation of

YAP (nuclear partitioning) via any of these physical cues is associated strongly with EC

activation, vascular inflammation, and atherosclerotic progression[3, 7, 8, 11, 15, 16, 25, 26]. As a result,

YAP/TAZ activity has been implicated in atherosclerotic progression as a key biological event

and specific downstream targets of its activity contribute to plaque progression[27, 28]. Altogether,

this paradigm highlights YAP/TAZ as major endothelial mechanical and biochemical sensors

important for maintaining homeostasis. Notably, YAP/TAZ responds to both stiffness and shear,

suggesting that the connection between the clinical paradigms of stiffness and endothelial

dysfunction or inflammation may be explained in part via dysregulated YAP activity, with shear

stress and substrate stiffness interacting to generate the biological response. Thus, we

hypothesized that increasing substrate stiffness affects the EC shear mechanoresponse by

upregulating YAP activity, connecting vascular stiffness with endothelial activation (causing atherosclerotic progression).

Testing this hypothesis and precisely controlling for all the physical parameters to study YAP activity is non-trivial[18, 20-22], and systems to study YAP mechanobiology are in clear demand[29]. Furthermore, there are relatively few studies which precisely isolate the interactions of these parameters in vessels to establish a mechanistic connection between them[30], and elucidating this further has several implications in cardiovascular medicine. Thus, to explore whether there exists a connection between the physical parameters of stiffness and shear stress via EC YAP mechanobiology, we employed organ-on-a-chip technology. Organ-on-a-chip (organ-chips) systems have emerged as biomimetic *in vitro* models of human physiology designed to reproduce physiologically-relevant environments and to replicate tissue- and organ-level functions[31-35]. Work from our group and others has shown that organ-chips may be an exceptional tool to isolate and elucidate the biological effects of a range of cellular, chemical, and physical parameters[32-34, 36]. These vessel-chips facilitate the study of endothelial pathology by supporting system interrogation wherein each degree of freedom may be allowed to vary individually[37, 38]. Currently, there are few engineered systems which are reported for the study of YAP/TAZ[39, 40], which focus either on the development of the system, cyclic strain, or developmental biology. Several microfluidic shearing systems exist which are focused on studying ECs with design and development ongoing[41-44], however, these systems do not currently incorporate relevant, interacting physiological forces (e.g. stiffness and shear stress) to study how they collaboratively influence endothelial biology. In this work, we employ a vessel-chip to

study the interaction of clinically relevant physical parameters (stiffness and shear) to yield novel biological insights into endothelial mechanobiology.

Our vessel-chip model integrates three-dimensional (3D) luminal geometry, dynamic range of uniform and oscillatory shear stress, and variable matrix stiffness that replicates the physiological and pathophysiological range of these parameters in the human vasculature[10, 11, 45-47] facilitating the study of how these parameters interact and influence the EC mechanoresponse. We extensively validate our model from a biological perspective to show that it captures the *in vivo* behavior of YAP/TAZ accurately in previously studied regimes while additionally exploring shear stress patterns not commonly addressed. We further tie the YAP behavior in the system to established biological paradigms, demonstrating EC inflammation under regimes which upregulate YAP activity, relevant modulation of gene expression, and confirm the findings via pharmacologic inhibition of YAP. Lastly, we vary shear stress and substrate stiffness together to explore how convoluting physical inputs affects ECs, in which we demonstrate that substrate stiffening results in upshifted YAP nuclear partitioning under high shear, connecting the two physical paradigms. We discuss several novel biological findings during validation and the implications of YAP in EC mechanobiology throughout. Holistically, this work demonstrates use of engineered organ-chip systems as tools to construct biology in a "bottom-up" fashion resulting in novel biological findings previously inaccessible via conventional methodology.

Materials and Methods

Channel Fabrication: Vessel-chips were fabricated according to our previous work[48]. Briefly, positive channels were designed in Solidworks®, acquired from OutputCity Inc., and

photolithographically printed onto silicon wafers (University Wafer Corp.). The upper chamber

of vessel-on-a-chip devices were fabricated via soft lithography using polydimethylsiloxane

(PDMS, Dow Corning) and then bonded to a borosilicate glass (BSG) slide or cover slip (75 mm

x 25 mm) which was either spin-coated with self-consistent PDMS (uniform channel) or left

uncoated for stiff BSG controls (stiffness studies). Bonding was performed following O_2 plasma

treatment (Thierry Zepto, Deiner Plasma) in a dedicated clean room.

Stiffness Measurements: Substrate stiffness was varied by changing the crosslinker

concentration of the PDMS formulations[49]. Compressive data was collected for the combination

of PDMS with 5%, 7.5%, and 10% by weight of crosslinker. First, samples were punched into 10

mm diameter discs using a biopsy punch and heights measured using digital calipers. Samples

were compressed to not greater than 20% of the measured height at a strain rate of 1 mm/min

utilizing an ADMET MTEST Quattro eXpert 7600 Single Column Testing System with a 25 lb

load cell. The raw data collected was processed into MS-Excel to calculate the compressive

moduli as the slope of the linear region of the strain vs. stress graph. For atomic force

microscopy validation studies on ECM functionalized and non-functionalized PDMS thin films,

a Catalyst Biomicroscope (Bruker) was employed. MLCT conical probes (0.01 N/m; Bruker

Nano) were used to measure elastic moduli pre- and post-ECM functionalization. The AFM

scanning frequency used was 1 Hz in PBS. All data was processed using Nanoscope Analysis

1.50r1 (Bruker). Sneddon's conical fitting was used on thin films, taking from 0-10%[50] of the

full AFM force curve for at least 15 technical replicates. Iterative outlier analysis was used to

remove any technical replicates which deviated strongly from the spread, and the group was

averaged to yield the stiffness of the PDMS film.

Cell Culture: Human umbilical venous endothelial cells (HUVECs, Lonza) were cultured in endothelial growth media (EGM-2, Lonza) using an endothelial cell supplement EGM-2-M (Lonza). Cell culture washes were performed using pH 7.2 phosphate buffered saline (PBS, Gibco), and cell passaging was performed using 1x 0.25% Trypsin-EDTA (Gibco). HUVECs used were all between p4 and p6, passage matched for each experiment.

Channel Functionalization and Lumenization: After fabrication of the Vessel-Chips, each channel was treated with O_2 plasma (PDC-32G, Harrick Plasma) for 5 minutes, and then an extracellular matrix (ECM) solution of 100 µg/mL rat tail collagen type I (Corning) and 50 µg/mL human fibronectin (Sigma Aldrich) was perfused through the channel and incubated for 30 minutes at 37°C, 5% CO_2. Plate controls reported were done on BSG cover slips, or 10% PDMS spin-coated glass cover slips using the same plasma treatment procedure and ECM solution. Afterwards, each channel/cover slip was then placed in an incubator at 37°C and 5% CO_2 for 30 minutes. The ECM solution was subsequently removed by perfusing EGM-2-M media through the chamber, or via washing of the cover slips. On the fully assembled vessel-chip devices, HUVECs were seeded onto the top and bottom faces of the chamber and allowed 1 hour for attachment. After the seeding period, the seeded vessel-on-a-chip devices were attached to a syringe pump (PHD ULTRA 4400, Harvard Apparatus) using a Luer curved dispenser tips (Qosina) and 20" tubing (0.094' ID, 0.145' OD; Qosina) and operated in suction mode. Media reservoirs were made from 5 mL syringes (BD). To allow for lumen formation, each chamber was then placed in shearing flow overnight at a flow rate of 1 µL/min before each experiment was conducted (post-lumenization; t = 0). For the quasistatic control, HUVECs were seeded and

cultured under extremely low shear (<2 µL/hour) using two 1-mL pipets as reservoirs for 48

hours such that cellular confluence was achieved.

Flow Rates: Flow rate shear stresses were calculated numerically using the finite element

method in Ansys Fluent v29R1 from Solidworks v19 models. Cell culture media (comparable to

water) was used as the fluid for modeling (density: 0.998 g/cm^3; viscosity: 0.001 Pa*s). A flow

rate of 1 µL/min was calculated to be 1.12 dynes/cm^2 (low/venous shear), and 10 µL/min was

calculated to be 11.2 dynes/cm^2 (high/arterial shear). Values are reported as exact calculations at

the center of the XZ planes (top/bottom wall shear) – distant from the corner. Disturbed flow was

induced via an oscillatory flow pattern of 1 or 10 µL/min, 2 seconds of withdrawal and 1 second

of infusion (100% duty cycle, 0.33 Hz) to deliver fresh media. Each of these regimens were run

for 3 hours and 6 hours after appropriate lumenization.

Verteporfin Treatment: Verteporfin was purchased from Millipore Sigma (≥94% HPLC) and

dissolved into a 1 mM stock in dimethyl sulfoxide (DMSO; Millipore Sigma) and stored at -

20°C until use. The stock solution was diluted into 2 mL of EGM-2-M media for the

corresponding experiment. Each concentration was supplemented with DMSO to ensure each

flow chamber received the same amount of DMSO regardless of dilution. Verteporfin was

introduced into the chamber in a dose-dependent manner. DMSO controls were media and the

total DMSO volume required for dilution only.

RNA Isolation and Gene Expression: HUVECs in each channel were trypsinized and cells

pelleted for RNA extraction and lysed with 10 minutes of detachment. Note that YAP is rapidly

inactivated upon trypsinization and gene expression is thus dependent on the half-life of the mRNA[51]; cells must be lysed quickly and RNA extraction begun immediately. RNA was extracted using an Arturus™ PicoPure™ RNA Extraction Kit (Applied Biosystems, Thermo Fisher Scientific). The cDNA was synthesized from the extracted RNA using a 5x iScript Reverse Transcriptase Supermix (Bio-Rad Laboratories, Inc.). The cDNA was then diluted to a volume of 100 μL for qPCR. For each qPCR reaction, a volume of 20 μL was used consisting of 10 μL of Power SYBR® Green Master Mix (Applied Biosystems, Thermo Fisher Scientific), 7 μL of H$_2$O (DNAse/RNAse free, molecular grade), 1 μL of the gene specific primer, and 2 μL of the sample cDNA. All primers were purchased as validated 20x SYBR® Green assays for glutaraldehyde 3-phosphate dehydrogenase (GAPDH), endothelial nitric oxide synthase (eNOS), connective tissue growth factor (CTGF), ankyrin repeat domain 1 (ANKRD1), intercellular adhesion molecule 1 (ICAM-1), vascular adhesion molecule 1 (VCAM-1), vascular endothelial growth factor receptor 2 (VEGFR2), and interleukin 6 (IL-6), (Bio-Rad Laboratories, Inc.). RT-qPCR was performed on a QuantStudio 12K Flex (Applied Biosystems, Life Technologies) with the following pre-set settings: 96-Fast Well Plate 0.1 mL, Relative Quantification (-$\Delta\Delta C_t$), SYBR® Green Reporter, and Standard Run Time. All gene expression results were reported as a fold change with respect to the denoted control and the housekeeping gene, GAPDH[52].

Immunohistochemistry: Each sample was fixed with 16% formaldehyde (Thermo Fisher Scientific) for 20 minutes at 4°C and then blocked and permeabilized with 2% bovine serum albumin (BSA, Sigma Aldrich) and 0.1% Triton X-100 (Thermo Fisher Scientific) in PBS (blocking buffer) for 1 hour at 4°C. Channels were then stained with either rabbit anti-YAP (Abcam), rabbit anti-VCAM1 (Abcam), rabbit anti-vWF (Dako), or mouse anti-CD144 (BD

Pharmigen) in blocking buffer (1:100) overnight at 4°C. Secondary staining was performed with

donkey anti-rabbit Alexa Fluor™ 555 (Invitrogen Molecular Probes, Thermo Fisher Scientific)

for 1 hour at room temperature. Actin was stained with phalloidin Alexa Fluor™ 488 (Invitrogen

Molecular Probes, Thermo Fisher Scientific). Nuclei were stained with 4',6'-diamidine-2'-

phenylindole dihydrochloride (DAPI, Roche Diagnostics).

Imaging and Analysis: Image acquisition was performed on an FLUOVIEW FV3000 confocal

microscope (Olympus Corporation). Analysis was performed on the associated software

(cellSens, Olympus Corporation) for YAP partitioning and circularity index by denoting regions

of interest and extracting the raw fluorescent values and measurements. YAP partitioning was

calculated as the nuclear YAP signal divided by the total cellular YAP signal for 60 cells.

Circularity index was calculated via $4\pi(area/perimeter^2)$ for 60 cells. Actin alignment images

were "grayscaled" in GIMP or ImageJ, and analysis was performed using the directionality

function in Fiji (ImageJ) using Fourier component analysis for 0° to 90°. The values were

reported in vector notation of the form($\mathbf{r}$,θ), where $\mathbf{r}$ corresponds to the relative density

(magnitude) of observations for a given angle calculated from the directionality function, and θ

(phase) is the angle itself. Thus, angular preferences are visualized as radial spikes or peaks, and

random organization is a radially homogenous distribution. Five or greater fields of view were

taken for each experimental condition in the study of actin alignment (indicated). Color mapping

was performed using OrientationJ[53].

Statistics and Data Visualization: All data was analyzed using either an appropriate Student's

t-Test or ANOVA with post-hoc Tukey's/Scheff's test. Statistical significance was set as p <

0.05, however all p-values are reported as their exact calculated value. All data visualization (except bar graphs) was performed in Python 3.7 using Matplotlib[54] with Seaborn packages. All scripts are available upon request; examples scripts are included in supplementary material.

Results and Discussion

Design of the Microfluidic Vessel-Chip System: In order to design a microfluidic culture environment conducive to studying endothelial mechanobiology, we first engineered the key physiologic parameters directly into the system and developed protocols to study ECs under different shear patterns. We employed the anatomy of a typical vessel-chip consisting of a microfluidic channel with a rectangular cross section providing a 3D culture environment for lumen formation (**Figure 1a-c**), where HUVECs cultured within the chamber formed a circular monolayer around the inner walls of the chamber (**Figure 1d**) after 18-hour incubation under a low shear rate (1 µL/min; **Figure 1e**). Next, to determine the shear regimes studied during the experimental portion of the protocol (t=0; **Figure 1e**), we used shear stresses and patterns which are known to be protective or inflammatory. To this end, we imposed a low shear (inflammatory) regime, a high shear regime (protective), and oscillatory versions of both (inflammatory)[5]. As the HUVEC response to shear has been extensively characterized[55-57], in that they respond favorably to arterial range shear (10 – 30 dynes/cm^2)[27], we selected a flow rate of 10 µL/min (11.2 dynes/cm^2) as our model of high shear. Conversely, low shear regimes (1-3 dynes/cm^2) are activating for endothelial cells – thus we selected a flow rate of 1 µL/min (1.12 dynes/cm^2) as our low shear regime (**Figure 1f**). To then model disturbed flow, we imposed a flow reversal pattern (oscillatory flow) to induce EC activation (**Figure 1g**), based on flow patterns known to cause activation[4, 5, 58]. Within our model, in order to deliver media over the course of the

experiment, a net positive flow vector was required, and thus the oscillatory regime displayed a frequency of 0.3 Hz (2 second withdrawal, 1 second infusion). 3D fluid modeling confirmed conventional laminar regimes within the cuboidal chamber and presence of a flow reversal in the oscillatory regimes which remained entirely laminar (**Figure 1h-i**). It is beneficial to note that in the context of the model, disturbed flow is isolated to being comprised of only flow reversal. While from a fluid mechanics perspective this is trivial, biologically the scenarios which activate ECs are complex, and several fundamental flow patterns may activate ECs, of which flow reversal is one. Other patterns such as recirculating flow also induce activation, and are classified as disturbed flow, and additionally disturbed flow need not be laminar[6, 17, 41, 59]. Lastly, to complete our protocol development, our experiment duration (t=0, **Figure 1e**) was set to follow the onset and stabilization of EC gene expression under shear, starting within an hour and stabilizing by 6 hours[60]. Thus, we selected an experimental duration of 6 hours. We confirmed this time point using gene expression of various shear sensitive genes (**Figure S1**).

Endothelial YAP/TAZ Mechanobiology in the Vessel-Chip: Our next goal was to establish that our vessel-chip model recapitulated known patterns of YAP/TAZ biology in endothelial cells: cytoplasmic retention under high, unidirectional (atheroprotective) laminar shear and nuclear partitioning when exposed to disturbed flow[15, 16]. We began by setting a quasistatic control baseline for HUVECs cultured on the chip (flow <2 µL/hour), as cells cultured in the vessel-chip require perfusion to remain alive and fully static state is not relevant. At these quasistatic conditions, partial YAP nuclear partitioning was observed (nuclear YAP/total YAP; **Figure S2a-b**). HUVECs elongated and aligned weakly along the flow vector, both attributable to culture under flow (**Figure S2c-d**). This baseline established, we moved to study and compare

physiologic/pathologic conditions. We examined YAP partitioning via immunofluorescence after 6 hours of the different flow regimes detailed earlier (**Figure 2a-b**). In all disturbed flow regimes (low shear 1 µL/min and both oscillatory regimes), we observed strong nuclear partitioning of YAP, while under the high atheroprotective regime, YAP was retained strongly in the cytoplasm (**Figure 2c**). We note that the quasistatic control YAP partitioning values were statistically identical to that of the oscillatory regimes (p = 0.9), indicating the strong influence of protective shear on YAP cytoplasmic retention and importance of fluid flow. Altogether, all parameters which conventionally classify as disturbed flow strongly induced YAP nuclear partitioning. Although this observation is consistent with previous studies[15, 16] reporting that disturbed flow results in YAP activation in ECs, we have added some greater resolution to the mechanosensing paradigm, as few studies have explored differences between unidirectional and oscillatory flow at low levels of shear stress. We observed that the flow pattern appears to be the dominant determinant of YAP localization in high shear regimes (10 µL/min unidirectional vs. oscillatory). By contrast, when the shear stress is low, ECs are comparably activated by unidirectional or oscillatory flow.

Within our vessel-chip model, we additionally observed common morphology changes associated with disturbed flow. HUVECs exposed to high shear became elongated, while in all disturbed flow regimes cells remained rounded (**Figure 2d**). Although EC exposed to both unidirectional regimes aligned primarily along the 0° flow vector, those exposed to high shear displayed a much more prominent alignment peak (Frequency peak: 1 µL/min=0.13 vs. 10 µL/min=0.23). HUVECs exposed to oscillatory flow regimes all displayed a blunted alignment (**Figure 2e**). Representative color mapping of actin alignment (from **Figure 2a**) demonstrates the

wide distribution of angles seen in the oscillatory regimes (**Figure 2f**). Taken together, our data

suggests that the key observations of *in vivo* YAP behavior are captured within the vessel-chip

system, while additionally facilitating novel findings pertaining to the relative influence that

shear stress magnitude and pattern have on endothelial activation. Moreover, morphological

characteristics of ECs subject to (disturbed) flow were readily captured and shown to be

consistent with current understanding[61, 62].

Endothelial Activation and Inflammation in the Vessel-Chip: In the context of vascular

mechanobiology, drawing connections between the detrimental mechanoresponse from disturbed

flow (YAP nuclear localization and increased activity) and the clinical implications

(atherosclerotic progression and vascular disease) would be vital to capture within our model to

ensure the mechanobiological changes parallel alterations in endothelial activation. Specifically,

does nuclear YAP partitioning (with disturbed flow) parallel endothelial activation and

inflammation? Accordingly, we selected an atheroprotective regime (unidirectional high shear)

and the corresponding disturbed flow pattern (oscillatory high shear), and assessed the relative

level of two molecules known to be induced under disturbed flow and integral to atherosclerotic

progression: vascular cell adhesion molecule 1 (VCAM-1) and von Willebrand Factor (vWF)[5, 63-68]. We observed reduced levels of both VCAM-1 and vWF when HUVECs were subject to

unidirectional high shear, whereas high oscillatory shear greatly increased the levels of both

VCAM-1 and vWF (**Figure 3a-d**), illustrating the connection between the EC mechanoresponse

and EC inflammatory activation.

Gene Expression Analysis: Subsequently, we examined gene expression of ECs subject to the various fluid shear stress parameters. The first two genes examined, connective tissue growth factor (CTGF) and ankyrin repeat domain 1 (ANKRD1) are downstream targets of YAP/TAZ activity known to be upregulated by its transcriptional co-activation[15, 16]. The second two genes, endothelial nitric oxide synthase (eNOS) and vascular endothelial growth factor receptor 2 (VEGFR2), are shear responsive genes[59, 69-74] not directly tied to YAP activity. Unidirectional high shear downregulated expression of CTGF compared to unidirectional low shear, however ANKRD1 remained relatively unchanged (**Figure 4a**). Under the conditions of high oscillatory shear, CTGF and ANKRD1 were both dramatically upregulated (**Figure 4b**), consistent with previous reports[15, 16]. By contrast, at low levels of shear stress, there was no difference between unidirectional and oscillatory shear stress in expression of CTGF and ANKRD1 (**Figure 4c**). Taken together, this data suggests than CTGF expression is highly sensitive to both the magnitude and pattern of shear stress. By contrast, the expression of ANKRD1 is not affected by difference in the magnitude of unidirectional shear stress, but is affected by the flow pattern at higher levels of shear stress. Notably, the sensitivity of CTGF to the magnitude of unidirectional shear stress has been previously reported[56]. Changes in other known mechanosensitive genes (eNOS and VEGFR2) were modest but in the expected directions (**Figure 4d-f**). Summarizing, these data confirm that our chip model replicates the known biological effects of laminar and disturbed flow (i.e. response of eNOS and VEGFR2) and provide new insights into the flow response of genes downstream of YAP/TAZ activation (i.e. CTGF and ANKRD1). Notably, CTGF is highly expressed in atherosclerotic plaques[75-77] and knockdown greatly reduces plaque progression[78]. This is consistent with our data that CTGF is upregulated by patterns of disturbed

flow, which hemodynamic condition is associated with sites in the vasculature that are predisposed to atherosclerosis.

Pharmacologic Inhibition of YAP Activity: To confirm the importance of YAP activity on the flow-mediated regulation of mechanosensitive genes, we employed verteporfin, a potent YAP inhibitor[79-82]. We assessed a dose response to verteporfin (0.125 – 1 µM; **Figure S4a-b**) and assessed YAP nuclear localization of treated cells subject to 10 µL/min oscillatory shear. We observed increasing cytoplasmic retention of YAP with increasing concentrations of verteporfin, with 1 µM verteporfin treatments resulting in cytoplasmic retention of YAP comparable to that of ECs subject to high unidirectional shear (**Figure 5a-b**). Notably, concentrations above 1 µM induced excessive cellular detachment (**Figure S4c**), which is attributable to verteporfin's ability to potently induce apoptosis and cell death at high concentrations[83]. Additionally, verteporfin treatment did not rescue cell circularity/morphology nor alignment (**Figure 5c-d** and **S4d**). As concentrations of 1 µM demonstrated the highest tractable cytoplasmic retention, we selected 1 µM as the concentration to examine inhibition of downstream YAP gene expression. Compared the DMSO controls (required for verteporfin solubility), verteporfin strongly suppressed expression of CTGF, however, strikingly ANKRD1 expression was not affected (**Figure 5e**). We note that this mirrors the finding of Wang et al.[16] when they reported pharmacological inhibition of c-Jun N-terminal kinase (downstream of YAP/TAZ activity) greatly modulated CTGF expression, but minimally affected ANKRD1[16]. Thus, this supports that CTGF is predominantly regulated by upstream YAP activity (and thus the EC mechanoresponse), however ANKRD1 is likely to be associated with other regulatory pathways. More generally, these pharmacological studies performed using the vessel-chip system in this manner demonstrate how chemical

intervention can influence and reverse the biological response to mechanical cues, and how

organ-chip systems support these preclinical and potentially translational studies in a controlled

manner.

Substrate Stiffness Impedes the Shear Mechanoresponse: As YAP is responsive to both

substrate stiffness and shear stress, we hypothesized that stiffening the substrate matrix impedes

the ability of ECs to fully respond to shear stress, upshifting YAP nuclear localization. The

stiffness of the PDMS substrate was modified by varying the crosslinker concentration[49]. Arterial

stiffnesses range from 50 kPa up to roughly 600 kPa[45-47]. Complicating this paradigm is that

diseased vasculature and atherosclerotic plaques have a significantly higher range of stiffnesses,

from 1 kPa up to 5 MPa[10, 11]. Thus, we explored a stiffness of the same order of magnitude as

those reported in normal muscular arteries (300-500 kPa; such as the coronary arteries)[12] as well

as stiffness in the range of atherosclerotic vessels (>1 MPa). Accordingly, we reduced the

crosslinker density to 7.5% (to yield 1 MPa) and to 5% (500 kPa); ECM functionalization did not

alter the PDMS materials properties (**Figure S5**). We subjected endothelial cells grown on these

matrices to unidirectional low or high shear and measured YAP localization (**Figure 6a-b**).

Consistent with our previous experiments, all low shear groups displayed elevated YAP nuclear

partitioning consistent with EC activation under flow. Furthermore, all high shear groups

displayed significantly decreased nuclear YAP localization. However, higher levels of stiffness

attenuated the effect of high shear to reduce YAP nuclear partitioning (**Figure 6c**), indicating

that stiff matrices impede the protective EC shear mechanoresponse. Also, of note, there was no

difference in the nuclear localization with increasing stiffness when shear stress was low. This

finding indicates that low shear stress (such as that found at sites of disturbed flow in the large

and medium arteries) is strongly activating and a dominant stimulator of YAP activity, EC

activation, and vascular inflammation. Interestingly, high shear was sufficient to induce YAP

cytoplasmic retention on borosilicate glass (Young's Modulus 64 GPa), displaying a value

statistically indistinguishable from the 10% PDMS (10% PDMS=0.32±0.1; BSG=0.32±0.1;

p=0.7), which suggests the influence of matrix stiffness on the shear mechanoresponse plateaus

past some highly stiff threshold (**Figure S6**). Altogether, this data suggests that ECs reside in a

complex physical environment where they balance different physical cues and respond

biologically to the convolution of the stimuli (**Figure 6d-e**). The protective signals from high

shear stress are attenuated by increasing matrix stiffness to a certain threshold, while low shear is

universally activating. Notably, this data supports a biological link associating matrix stiffness

and flow patterns to EC dysfunction, inflammation, and atherosclerotic progression, consistent

with clinical data.

Conclusions

Here, our report describes the use of a vessel-chip model to arrive at novel understandings of the

interaction of physiological forces which conventional methods or models may not facilitate.

This type of "bottom-up" engineering approach to biology, combined with insights from current

in vitro and *in vivo* models, may provide a more comprehensive understanding of forces acting

on cells in a concerted fashion to result in a single biological response.

In the context of vascular mechanobiology, our vessel-chip model yielded several new insights

into the physical cues which govern EC health and homeostasis. First, our data reveals that shear

stress magnitudes and patterns are a dominant signal in EC phenotype maintenance. The most

dramatic differences were observed between unidirectional and oscillatory flow patterns at high

levels of shear. Interestingly, the pattern of flow (unidirectional v. oscillatory) did not

appreciably modulate gene expression when ECs were subject to low levels of shear. Thus, low

levels of shear (which promote atherosclerosis in the arterial circulation) dominate over the flow

pattern with respect to EC signaling. Gene expression analysis across flow regimes and inhibitor

studies highlighted CTGF as a highly sensitive measure of the EC mechanoresponse to shear and

flow pattern. CTGF was upregulated with disturbed flow, consistent with its increased

expression in atherosclerotic vessels. By contrast, ANKRD1 was only affected by the flow

pattern at high levels of shear stress. Verteporfin studies confirmed that CTGF but not ANKRD1

is significantly downregulated by YAP inhibition, emphasizing the distinction between these

genes.

The most significant finding of this report is the interaction of substrate stiffness with shear

stress to modulate the EC YAP mechanoresponse. Here, we observed that increasing the

substrate stiffness increased the levels of YAP localized to the nucleus under high shear,

however low shear was strongly activating across varying stiffnesses. Our work is consistent

with prior studies associating coronary wall stiffness and shear patterns with development of

atherosclerosis[10-12]. Indeed, the data suggests a feedforward mechanism of EC activation and

atherosclerotic progression (**Figure 6f**) where some inciting event (either physical or chemical[6, 84]) induces YAP activation in ECs. This, in turns, causes endothelial activation and vascular

inflammation, as reported previously[15, 16]. The endothelial activation and vascular inflammation

then drive atherosclerotic progression, which may further stiffen the vascular architecture,

activating YAP further. Kohn and colleagues observed that stiffer substrates resulted in lower

eNOS production and increased RhoA activation[30], the latter of which interacts with

YAP/TAZ[85]. Together, their work and ours strongly suggest that matrix stiffness attenuates the

endothelial response to physiological shear stress. The combination of a decrease of eNOS (also

atherogenic[7]) and increases in RhoA and YAP/TAZ activity all serve to suggest that matrix

stiffening is not only a correlative consequence, but a cause of vascular disease. Indeed, other

recent reports indicate that YAP activation is associated with vessel stiffening in the context of

pulmonary hypertension[86-88], though do not explore fluid shear stress as deeply.

There are model limitations and interpretation qualifiers important to discuss. Our current vessel-

chip model does not incorporate strain, which is known to activate YAP activity as well[39].

Furthermore, we have not incorporated a vascular smooth muscle cell layer in our model, which

also contributes to vascular disease[89, 90]. Thus, some of the biological implications of our model

findings require additional study to incorporate the interaction of these biological variables with

stiffness, shear stress, and flow patterns. Also of note is that the ECM chemical composition

itself influences EC behavior[91], which was not a variable considered in our work. We also

assumed that the matrix is a uniform, isotropic material, however, blood vessels are composite

and anisotropic[46]. Lastly, our work focuses on modeling mechanobiological response in the

arterial circulation (using HUVECs) which may not be entirely reflective of the venous

mechanoresponse. As an example, recent work, including our own, highlights that low (~1

dyne/cm^2) recirculating flow in vein leaflets is protective[92, 93], rather than activating. Thus, our

conclusions are only appropriately applied to arterial biology while venous mechanobiology

requires more investigation.

Nonetheless, we believe the methods and resulting conclusions emphasize how engineered

organ-chip models can be used in such a manner as to draw upon biological knowledge and

facilitate new findings. As evidenced by the work here, organ-chip systems support biological

inquiry that fills the gaps between the *in vitro* models and animal models. Further extension or

applications of this work include system sophistication to incorporate additional geometries or

cellular layers to study an additional interface, or the inclusion of iPSC-derived ECs or diseased

cell models to study perturbations of the shear response induced by internal, cellular dysfunction.

Conflicts of interest/Disclosures

The authors declare the following financial interests/personal relationships which may be

considered as potential competing interests: Prof. Guiseppi-Elie is founder and scientific director

References

1. D. E. Ingber, *Ann Med*, 2003, **35**, 564-577.
2. J. Ando and K. Yamamoto, *Circ J*, 2009, **73**, 1983-1992.
3. K. S. Cunningham and A. I. Gotlieb, *Lab Invest*, 2005, **85**, 9-23.
4. S. Chien, *Annals of biomedical engineering*, 2008, **36**, 554-562.
5. J.-J. Chiu and S. Chien, *Physiological reviews*, 2011, **91**, 327-387.
6. A. Dominic, P. Banerjee, D. J. Hamilton, N.-T. Le and J.-i. Abe, *Redox Biology*, 2020, 101614.
7. J. P. Cooke, *Proc Natl Acad Sci U S A*, 2003, **100**, 768-770.
8. N. M. van Popele, D. E. Grobbee, M. L. Bots, R. Asmar, J. Topouchian, R. S. Reneman, A. P. Hoeks, D. A. van der Kuip, A. Hofman and J. C. Witteman, *Stroke*, 2001, **32**, 454-460.
9. T. T. van Sloten, M. T. Schram, K. van den Hurk, J. M. Dekker, G. Nijpels, R. M. Henry and C. D. Stehouwer, *Journal of the American College of Cardiology*, 2014, **63**, 1739-1747.
10. J. Ohayon, P. Teppaz, G. Finet and G. Rioufol, *Coronary artery disease*, 2001, **12**, 655-663.
11. J. Ohayon, S. K. Yazdani, M. Malvè, A. M. Gharib, A. Garcia, G. Finet and R. I. Pettigrew, in *Biomechanics of Living Organs*, Elsevier, 2017, pp. 193-213.
12. J. Ohayon, A. M. Gharib, A. Garcia, J. Heroux, S. K. Yazdani, M. Malvè, P. Tracqui, M.-A. Martinez, M. Doblare and G. Finet, *American Journal of Physiology-Heart and Circulatory Physiology*, 2011, **301**, H1097-H1106.
13. C. Palombo and M. Kozakova, *Vascular pharmacology*, 2016, **77**, 1-7.
14. A. Totaro, T. Panciera and S. Piccolo, *Nat Cell Biol*, 2018, **20**, 888-899.
15. K. C. Wang, Y. T. Yeh, P. Nguyen, E. Limqueco, J. Lopez, S. Thorossian, K. L. Guan, Y. J. Li and S. Chien, *Proc Natl Acad Sci U S A*, 2016, **113**, 11525-11530.
16. L. Wang, J. Y. Luo, B. Li, X. Y. Tian, L. J. Chen, Y. Huang, J. Liu, D. Deng, C. W. Lau, S. Wan, D. Ai, K. K. Mak, K. K. Tong, K. M. Kwan, N. Wang, J. J. Chiu, Y. Zhu and Y. Huang, *Nature*, 2016, **540**, 579-582.
17. S. Xu, M. Koroleva, M. Yin and Z. G. Jin, *Transl Res*, 2016, **176**, 18-28 e12.
18. S. Piccolo, S. Dupont and M. Cordenonsi, *Physiol Rev*, 2014, **94**, 1287-1312.
19. M. Aragona, T. Panciera, A. Manfrin, S. Giulitti, F. Michielin, N. Elvassore, S. Dupont and S. Piccolo, *Cell*, 2013, **154**, 1047-1059.
20. S. Dupont, in *The Hippo Pathway*, Springer, 2019, pp. 183-202.
21. S. Dupont, *Exp Cell Res*, 2016, **343**, 42-53.
22. S. Dupont, L. Morsut, M. Aragona, E. Enzo, S. Giulitti, M. Cordenonsi, F. Zanconato, J. Le Digabel, M. Forcato, S. Bicciato, N. Elvassore and S. Piccolo, *Nature*, 2011, **474**, 179-183.
23. W. Hong and K. L. Guan, *Semin Cell Dev Biol*, 2012, **23**, 785-793.
24. J. S. Warren, Y. Xiao and J. M. Lamar, *Cancers*, 2018, **10**, 115.
25. K. S. Heo, K. Fujiwara and J. Abe, *Mol Cells*, 2014, **37**, 435-440.

26.   H. L. Kim and S. H. Kim, *Front Cardiovasc Med*, 2019, **6**, 41.
27.   S. L. Diamond, *Circ Res*, 2016, **118**, 1348-1362.
28.   T. Panciera, L. Azzolin, M. Cordenonsi and S. Piccolo, *Nat Rev Mol Cell Biol*, 2017, **18**, 758-770.
29.   G. Brusatin, T. Panciera, A. Gandin, A. Citron and S. Piccolo, *Nature materials*, 2018, **17**, 1063-1075.
30.   J. C. Kohn, D. W. Zhou, F. Bordeleau, A. L. Zhou, B. N. Mason, M. J. Mitchell, M. R. King and C. A. Reinhart-King, *Biophysical journal*, 2015, **108**, 471-478.
31.   B. Zhang, A. Korolj, B. F. L. Lai and M. Radisic, *Nature Reviews Materials*, 2018, **3**, 257-278.
32.   K. Gold, A. K. Gaharwar and A. Jain, *Biomaterials*, 2019, **196**, 2-17.
33.   K. H. Benam, S. Dauth, B. Hassell, A. Herland, A. Jain, K. J. Jang, K. Karalis, H. J. Kim, L. MacQueen, R. Mahmoodian, S. Musah, Y. S. Torisawa, A. D. van der Meer, R. Villenave, M. Yadid, K. K. Parker and D. E. Ingber, *Annu Rev Pathol*, 2015, **10**, 195-262.
34.   S. N. Bhatia and D. E. Ingber, *Nat Biotechnol*, 2014, **32**, 760-772.
35.   N. S. Bhise, J. Ribas, V. Manoharan, Y. S. Zhang, A. Polini, S. Massa, M. R. Dokmeci and A. Khademhosseini, *Journal of Controlled Release*, 2014, **190**, 82-93.
36.   A. D. van der Meer, V. V. Orlova, P. ten Dijke, A. van den Berg and C. L. Mummery, *Lab Chip*, 2013, **13**, 3562-3568.
37.   A. Jain, A. D. van der Meer, A. L. Papa, R. Barrile, A. Lai, B. L. Schlechter, M. A. Otieno, C. S. Louden, G. A. Hamilton, A. D. Michelson, A. L. Frelinger, 3rd and D. E. Ingber, *Biomed Microdevices*, 2016, **18**, 73.
38.   N. K. R. Pandian, R. G. Mannino, W. A. Lam and A. Jain, *Current Opinion in Biomedical Engineering*, 2018, **5**, 29-34.
39.   V. Lundin, W. W. Sugden, L. N. Theodore, P. M. Sousa, A. Han, S. Chou, P. J. Wrighton, A. G. Cox, D. E. Ingber and W. Goessling, *Developmental Cell*, 2020.
40.   G. Vázquez-Victorio, C. Peto-Gutiérrez, B. Díaz-Bello, M. Cano-Jorge, D. Pérez-Calixto, A. Jiménez-Escobar, S. Espinosa-Matías, R. L. Martínez, R. Courson and L. Malaquin, *Lab on a Chip*, 2019, **19**, 3512-3525.
41.   F. Tovar-Lopez, P. Thurgood, C. Gilliam, N. Nguyen, E. Pirogova, K. Khoshmanesh and S. Baratchi, *Frontiers in bioengineering and biotechnology*, 2019, **7**, 81.
42.   M. Mohammed, P. Thurgood, C. Gilliam, N. Nguyen, E. Pirogova, K. Peter, K. Khoshmanesh and S. Baratchi, *Analytical chemistry*, 2019, **91**, 12077-12084.
43.   M. Inglebert, L. Locatelli, D. Tsvirkun, P. Sinha, J. A. Maier, C. Misbah and L. Bureau, *Biomicrofluidics*, 2020, **14**, 024115.
44.   P. Thurgood, S. A. Suarez, E. Pirogova, A. R. Jex, K. Peter, S. Baratchi and K. Khoshmanesh, *Small*, 2020, 2003612.
45.   R. Akhtar, M. J. Sherratt, J. K. Cruickshank and B. Derby, *Materials Today*, 2011, **14**, 96-105.
46.   C. F. Guimarães, L. Gasperini, A. P. Marques and R. L. Reis, *Nature Reviews Materials*, 2020, 1-20.
47.   A. P. Ebrahimi, *Journal of vascular and interventional neurology*, 2009, **2**, 155.
48.   T. Mathur, K. A. Singh, R. P. NK, S. H. Tsai, T. W. Hein, A. K. Gaharwar, J. M. Flanagan and A. Jain, *Lab Chip*, 2019, **19**, 2500-2511.
49.   A. Mata, A. J. Fleischman and S. Roy, *Biomedical microdevices*, 2005, **7**, 281-293.
50.   N. Gavara and R. S. Chadwick, *Nature nanotechnology*, 2012, **7**, 733-736.
51.   B. Zhao, L. Li, L. Wang, C.-Y. Wang, J. Yu and K.-L. Guan, *Genes & development*, 2012, **26**, 54-68.
52.   R. D. Barber, D. W. Harmer, R. A. Coleman and B. J. Clark, *Physiological genomics*, 2005, **21**, 389-395.
53.   Z. Püspöki, M. Storath, D. Sage and M. Unser, in *Focus on Bio-Image Informatics*, Springer, 2016, pp. 69-93.
54.   J. D. Hunter, *Computing in Science & Engineering*, 2007, **9**, 90-95.

55. H. Inoguchi, T. Tanaka, Y. Maehara and T. Matsuda, *Biomaterials*, 2007, **28**, 486-495.
56. S. M. McCormick, S. G. Eskin, L. V. McIntire, C. L. Teng, C.-M. Lu, C. G. Russell and K. K. Chittur, *Proceedings of the National Academy of Sciences*, 2001, **98**, 8955-8960.
57. T. Nagel, N. Resnick, W. J. Atkinson, C. F. Dewey and M. A. Gimbrone, *The Journal of clinical investigation*, 1994, **94**, 885-891.
58. D. C. Chappell, S. E. Varner, R. M. Nerem, R. M. Medford and R. W. Alexander, *Circulation research*, 1998, **82**, 532-539.
59. K. S. Heo, B. C. Berk and J. Abe, *Antioxid Redox Signal*, 2016, **25**, 435-450.
60. N. E. Ajami, S. Gupta, M. R. Maurya, P. Nguyen, J. Y. Li, J. Y. Shyy, Z. Chen, S. Chien and S. Subramaniam, *Proc Natl Acad Sci U S A*, 2017, **114**, 10990-10995.
61. S. Zhao, A. Suciu, T. Ziegler, J. E. Moore Jr, E. Bürki, J.-J. Meister and H. R. Brunner, *Arteriosclerosis, thrombosis, and vascular biology*, 1995, **15**, 1781-1786.
62. C. M. Potter, M. H. Lundberg, L. S. Harrington, C. M. Warboys, T. D. Warner, R. E. Berson, A. V. Moshkov, J. Gorelik, P. D. Weinberg and J. A. Mitchell, *Arteriosclerosis, thrombosis, and vascular biology*, 2011, **31**, 384-391.
63. P. Doddapattar, N. Dhanesha, M. R. Chorawala, C. Tinsman, M. Jain, M. K. Nayak, J. M. Staber and A. K. Chauhan, *Arteriosclerosis, thrombosis, and vascular biology*, 2018, **38**, 520-528.
64. P. S. Tsao, R. Buitrago, J. R. Chan and J. P. Cooke, *Circulation*, 1996, **94**, 1682-1689.
65. P. S. Tsao, R. Buitrago, J. R. Chan and J. P. Cooke, *Circulation*, 1996, **94**, 1682-1689.
66. S.-J. Hwang, C. M. Ballantyne, A. R. Sharrett, L. C. Smith, C. E. Davis, A. M. Gotto Jr and E. Boerwinkle, *Circulation*, 1997, **96**, 4219-4225.
67. M. I. Cybulsky, K. Iiyama, H. Li, S. Zhu, M. Chen, M. Iiyama, V. Davis, J.-C. Gutierrez-Ramos, P. W. Connelly and D. S. Milstone, *The Journal of clinical investigation*, 2001, **107**, 1255-1262.
68. K. Ley and Y. Huo, *The Journal of clinical investigation*, 2001, **107**, 1209-1210.
69. E. Tzima, M. Irani-Tehrani, W. B. Kiosses, E. Dejana, D. A. Schultz, B. Engelhardt, G. Cao, H. DeLisser and M. A. Schwartz, *Nature*, 2005, **437**, 426-431.
70. J. L. Tuttle, R. D. Nachreiner, A. S. Bhuller, K. W. Condict, B. A. Connors, B. P. Herring, M. C. Dalsing and J. L. Unthank, *American Journal of Physiology-Heart and Circulatory Physiology*, 2001, **281**, H1380-H1389.
71. I. Fleming, B. Fisslthaler, M. Dixit and R. Busse, *Journal of cell science*, 2005, **118**, 4103-4111.
72. Z.-G. Jin, H. Ueba, T. Tanimoto, A. O. Lungu, M. D. Frame and B. C. Berk, *Circulation research*, 2003, **93**, 354-363.
73. E. Gee, M. Milkiewicz and T. L. Haas, *Journal of cellular physiology*, 2010, **222**, 120-126.
74. P. Nigro, J.-i. Abe and B. C. Berk, *Antioxidants & redox signaling*, 2011, **15**, 1405-1414.
75. W.-H. Fan, M. Pech and M. J. Karnovsky, *European journal of cell biology*, 2000, **79**, 915-923.
76. I. Cicha, A. Yilmaz, M. Klein, D. Raithel, D. R. Brigstock, W. G. Daniel, M. Goppelt-Struebe and C. D. Garlichs, *Arteriosclerosis, thrombosis, and vascular biology*, 2005, **25**, 1008-1013.
77. I. Cicha, A. Yilmaz, Y. Suzuki, N. Maeda, W. G. Daniel, M. Goppelt-Struebe and C. D. Garlichs, *Clinical hemorheology and microcirculation*, 2006, **35**, 203-206.
78. N. Niu, S. Xu, Y. Xu, P. J. Little and Z.-G. Jin, *Trends in pharmacological sciences*, 2019, **40**, 253-266.
79. C. Wang, X. Zhu, W. Feng, Y. Yu, K. Jeong, W. Guo, Y. Lu and G. B. Mills, *American journal of cancer research*, 2016, **6**, 27.
80. H. Wei, F. Wang, Y. Wang, T. Li, P. Xiu, J. Zhong, X. Sun and J. Li, *Cancer science*, 2017, **108**, 478-487.
81. J. Feng, J. Gou, J. Jia, T. Yi, T. Cui and Z. Li, *OncoTargets and therapy*, 2016, **9**, 5371.
82. K. Brodowska, A. Al-Moujahed, A. Marmalidou, M. M. zu Horste, J. Cichy, J. W. Miller, E. Gragoudas and D. G. Vavvas, *Experimental eye research*, 2014, **124**, 67-73.
83. Y.-W. Ma, Y.-Z. Liu and J.-X. Pan, *American journal of cancer research*, 2016, **6**, 2816.
84. A. Dominic, D. Hamilton and J.-i. Abe, *Journal of Thrombosis and Thrombolysis*, 2020, 1-6.

85.   G. Sorrentino, N. Ruggeri, V. Specchia, M. Cordenonsi, M. Mano, S. Dupont, A. Manfrin, E. Ingallina, R. Sommaggio and S. Piazza, *Nature cell biology*, 2014, **16**, 357-366.
86.   T. Bertero, K. A. Cottrill, Y. Lu, C. M. Haeger, P. Dieffenbach, S. Annis, A. Hale, B. Bhat, V. Kaimal, Y. Y. Zhang, B. B. Graham, R. Kumar, R. Saggar, R. Saggar, W. D. Wallace, D. J. Ross, S. M. Black, S. Fratz, J. R. Fineman, S. O. Vargas, K. J. Haley, A. B. Waxman, B. N. Chau, L. E. Fredenburgh and S. Y. Chan, *Cell Rep*, 2015, **13**, 1016-1032.
87.   T. Bertero, W. M. Oldham, K. A. Cottrill, S. Pisano, R. R. Vanderpool, Q. Yu, J. Zhao, Y. Tai, Y. Tang and Y.-Y. Zhang, *The Journal of clinical investigation*, 2016, **126**, 3313-3335.
88.   P. B. Dieffenbach, C. M. Haeger, A. M. F. Coronata, K. M. Choi, X. Varelas, D. J. Tschumperlin and L. E. Fredenburgh, *American Journal of Physiology-Lung Cellular and Molecular Physiology*, 2017, **313**, L628-L647.
89.   R. Ross and J. A. Glomset, *Science*, 1973, **180**, 1332-1339.
90.   D. Gomez and G. K. Owens, *Cardiovascular research*, 2012, **95**, 156-164.
91.   E. W. Young, A. R. Wheeler and C. A. Simmons, *Lab on a Chip*, 2007, **7**, 1759-1766.
92.   J. D. Welsh, M. H. Hoofnagle, S. Bamezai, M. Oxendine, L. Lim, J. D. Hall, J. Yang, S. Schultz, J. D. Engel and T. Kume, *The Journal of clinical investigation*, 2019, **129**.
93.   N. K. Rajeeva Pandian, B. K. Walther, R. Suresh, J. P. Cooke and A. Jain, *Small*, 2020, **16**, 2003401.

FIGURE CAPTIONS

Figure 1: Fabrication of the vessel-chip microfluidic device for endothelial mechanobiology and preliminary quantification. **a** details the parts of the device bonded together to form a microfluidic channel. The PDMS upper is fabricated via soft-lithography from a positive master mold. The bottom is a glass slide which is left untreated (stiff control) or spin-coated with PDMS to make a fully coated device. The upper and the lower parts are both O_2 plasma treated and then bonded together and placed under weight (500 g or greater) for 30 minutes. **b** lays out the dimensions of the channel. Each channel is 2 cm long, has a height of 75 μm, and a width of 200 μm. The PDMS upper comprises the "top" face of the channel, while the bottom glass slide is the "bottom;" these faces are referred to when seeding cells in the device as both faces are seeded prior to experimentation. **c** are pictures of a fully fabricated device. **d** is a representative confocal maximum Z-image of a HUVEC lumen formed on the device using this protocol (Flow Rate: 10 μL/min). **e** is a graphical schematic of the cell culture protocol used for each experiment. After bonding, devices are O_2 plasma treated again and perfused with an ECM matrix (100 μg/mL collagen type I + 50 μg/mL fibronectin) and incubated at 37°C, 5% CO_2 for 30 minutes in a cell culture incubator. After the incubation was done, endothelial media (EGM-2) was perfused through the channel to remove excess matrix protein. HUVECs were then seeded on each face. To seed a face, cells were suspended in media and perfused through the channel. The channel was then placed in an incubator for 1 hour to let the cells attach, either right side up to seed the bottom face, or upside down to seed the top face (2 hours total seeding time). After seeding and cell attachment was complete, the channels were placed under perfusion (1 μL/min) for 18 hours to allow for cell proliferation and

lumen formation (lumenization). After the 18-hour lumenization was complete, different shear stresses and patterns were applied for the time required for each experiment. 3-dimensional computation fluid analysis of the applied wall shear stress based on the flow rate with corresponding physiological ranges are shown in **f**, while **g** details the oscillatory flow pattern used to induce activation (0.3 Hz cycle, 2 seconds withdraw, 1 second infuse). Flow velocity heatmap profiles are shown in **h** for the unidirectional regimes and the corresponding flow rate, and **i** details the velocity profile during an oscillatory cycle, showing the 1-dimensional change in flow direction and magnitude.

Figure 2: YAP mechanobiological model validation of the vessel-chip system for studying endothelial mechanobiology. In **a** are representative fields of view within the vessel-on-a-chip device for 1 µL/min, oscillatory 1 µL/min, 10 µL/min, and oscillatory 10 µL/min flow. Cells were stained for nuclei (DAPI, blue), actin (phalloidin, green,) and YAP (red). Oscillatory flow was induced by alternating between withdrawal (2 seconds) and infuse (1 second). **b** is a Z-stack image of a section of a vessel-on-a-chip showing lumen formation (10 µL/min). Scale bars in **a** and **b** are all 50 µm. YAP partitions for each group are: 1 µL/min: 0.37 ± 0.08; oscillatory 1 µL/min: 0.42 ± 0.1; 10 µL/min: 0.23 ± 0.08; oscillatory 10 µL/min: 0.43 ± 0.11 (**c**). The cellular morphology (circularity) is quantified in **d**. Circularity is defined as $4\pi(\text{area}/\text{perimeter}^2)$ and is valued from 0 to 1. Indices closer to 1 indicate more circular cell morphology, while elongated cells have indices closer to 0. CSI measured for the flow fields are: 1 µL/min: 0.67 ± 0.11; oscillatory 1 µL/min: 0.67 ± 0.11; 10 µL/min: 0.51 ± 0.11; oscillatory 10 µL/min: 0.64 ± 0.16. Directionality assays based on actin alignment detailing how HUVECs align along the flow vector within the fluidic chamber under the different shear regimens/patterns are shown in **e**. Data is visualized in the form of (r,θ) − r is the normalized density of actin filaments aligned at each angle, θ. Higher values of r for a given θ indicate increasing alignment. For 10 µL/min, HUVECs aligned strongly along the flow vector, while the effect was evident but not as strong in the 1 µL/min regime. HUVECs in both oscillatory flow fields showed a markedly decreased alignment distribution around the flow vector. Color maps showing the gradient of actin alignment (from the representative actin images in **a**) are visualized in **f** using OrientationJ. For YAP partition experiments and CSI experiments, n=60 cells. Alignment polar histogram plots are comprised of an average of 5-6 fields of view, directionality calculated from 0° to 90° binned 15 times in ImageJ. Statistics performed using a single factor ANOVA with post-hoc Tukey's test for significance. Each p-value between groups is reported natively as calculated, significance taken at $p < 0.05$. All values reported as mean ± standard deviation.

Figure 3: Endothelial activation studies between the different shear regimes. In order to establish the system parameters causing activation of YAP correlate to endothelial activation, 2 markers of endothelial inflammation (VCAM-1 and vWF) were examined under the laminar and oscillatory flow conditions. For both markers, oscillatory flow patterns resulted in marked intensity increases for VCAM-1 (**a-b**, Fluorescence: 10 µL/min – 2.4 ± 0.8 AUx10^3/µm^2, Oscillatory 10 µL/min – 7.1 ± 2 AUx10^3/µm^2) and vWF (**c-d**, Fluorescence: 10 µL/min – 3.1 ± 2 AUx10^3/µm^2, Oscillatory 10 µL/min – 17 ± 5 AUx10^3/µm^2). For VCAM-1, n=74 cells; for vWF, n=69 cells. Statistical analysis was performed using an unpaired Student's t-test, significance taken at $p < 0.05$. Data is reported as the normalized intensity (to cellular area), mean ± standard deviation.

Figure 4: Gene expression for key mechanosensitive genes were selected as transcriptional readouts (CTGF, ANKRD1, eNOS, and VEGFR2). CTGF expression was significantly decreased from 1 µL/min to 10 µL/min (**a**, FC = 0.6) while ANKRD1 was not changed (FC = 1.1). However, oscillatory 10 µL/min vs. 10 µL/min displayed a marked upregulation of both CTGF and ANKRD1 (**b**, respectively FC = 5.9 and FC = 3.3). Conversely, expression of CTGF and ANKRD1 in the oscillatory 1 µL/min vs. 1 µL/min regime was not changed (**b**, FC = 0.97 and FC = 0.76). With regards to eNOS and VEGFR2, from 1 µL/min to 10 µL/min, eNOS was not appreciably changed, though VEGFR2 saw modest upregulation (**d**, FC = 1.4 and FC = 2.0, respectively). Oscillatory 10 µL/min vs. 10 µL/min shown downward trends for both genes (**e**, FC = 0.67 and FC = 0.83) without reaching significance. Oscillatory 1 µL/min compared to 1 µL/min showed (**f**, FC = 1.0 and FC = 1.4). Verteporfin immunofluorescence (for nuclei (DAPI, blue), actin (phalloidin, green,) and YAP (red), **k**) showed decreasing YAP nuclear partitioning in the 1 µM groups vs. DMSO controls (DMSO: 0.46 ± 0.1; 1 µM: 0.30 ± 0.1, **l**). Gene expression analysis of CTGF and ANKRD1 post-verteporfin treatment (**m**) showed significant downregulation of CTGF (FC = 0.11) and insignificant modulation of ANKRD1 (FC = 0.70). For **a** and **d** CTGF, ANKRD1, and eNOS, n=7; all other genes performed n=4. Statistical analysis was performed on the ddCts for each group using an unpaired Student's t-test. All p-values are reported natively, significance taken at $p < 0.05$. Values are reported as FC. GAPDH was selected as the housekeeping gene for all experiments.

Figure 5: Verteporfin immunofluorescence (for nuclei (DAPI, blue), actin (phalloidin, green,) and YAP (red), **a**) showed decreasing YAP nuclear partitioning in the 1 µM group vs. DMSO control (DMSO: 0.46 ± 0.1; 1 µM: 0.30 ± 0.1, **b**). Verteporfin treatment did not rescue cellular morphology or alignment under oscillatory flow (**c-d**). Cell circularity indices for the DMSO and 1 µM Verteporfin groups were respectively 0.67 ± 0.1 and 0.71 ± 0.1. Gene expression analysis of CTGF and ANKRD1 post-verteporfin treatment (**e**) showed significant downregulation of CTGF (FC = 0.11) and insignificant modulation of ANKRD1 (FC = 0.70). Verteporfin treatment IF and circularity performed on n>59 cells. YAP partition is defined as (nuclear YAP/total YAP). Circularity is defined as 4π(area/perimeter^2) and is valued from 0 to 1. Alignment polar histogram plots are comprised of an average of 4-5 fields of view, directionality calculated from 0° to 90° binned 15 times in ImageJ. Data is visualized in the form of (r,θ). Higher values of r for a given θ indicate increasing alignment in that direction. Gene expression performed n=4. Statistical analysis

was performed on the calculated normalized IF values or ddCts for each group using an unpaired Student's t-test. All p-values are reported natively, significance taken at $p < 0.05$. Values are reported as circularity, FC, or normalized intensity, mean ± standard deviation. GAPDH was selected as the housekeeping gene for all experiments.

Figure 6: Varying device stiffness to modulate the HUVEC endothelial mechanoresponse. Experiments were performed in devices made form the varied crosslinker concentrations of 5%, 7.5%, and 10% and under the unidirectional shear regimes of 1 µL/min and 10 µL/min. Cells were stained for nuclei (DAPI, blue), actin (phalloidin, green,) and YAP (red), shown in **a-b**. Across the 1 µL/min groups, YAP partitioning was not affected by substrate stiffness (5%: 0.42 ± 0.1; 7.5%: 0.38 ± 0.1; 10%: 0.39 ± 0.1), while those subject to 10 µL/min showed increasing YAP partition as the substrate stiffened (5%: 0.25 ± 0.1; 7.5%: 0.29 ± 0.1; 10%: 0.32 ± 0.1, **c**). YAP nuclear partitioning between the 1 µL/min and 10 µL/min groups were significantly different between any 2 groups from different shear regimes. This suggests that ECs respond to a variety of mechanical cues which can either be protective or inflammatory (**d-e**). The physical regimes of stiffness and shear stress may be connected via YAP mechanobiology in a feedforward manner where an initial incident can result in propagating stiffening and YAP activity (**f**). For the 1 µL/min groups, n = 56 cells, for the 10 µL/min groups, n = 71-73 cells). Statistics performed using a single factor ANOVA with post-hoc Tukey's test for significance. Each p-value between groups is reported natively as calculated, significance taken at $p < 0.05$. All values reported as mean ± standard deviation.
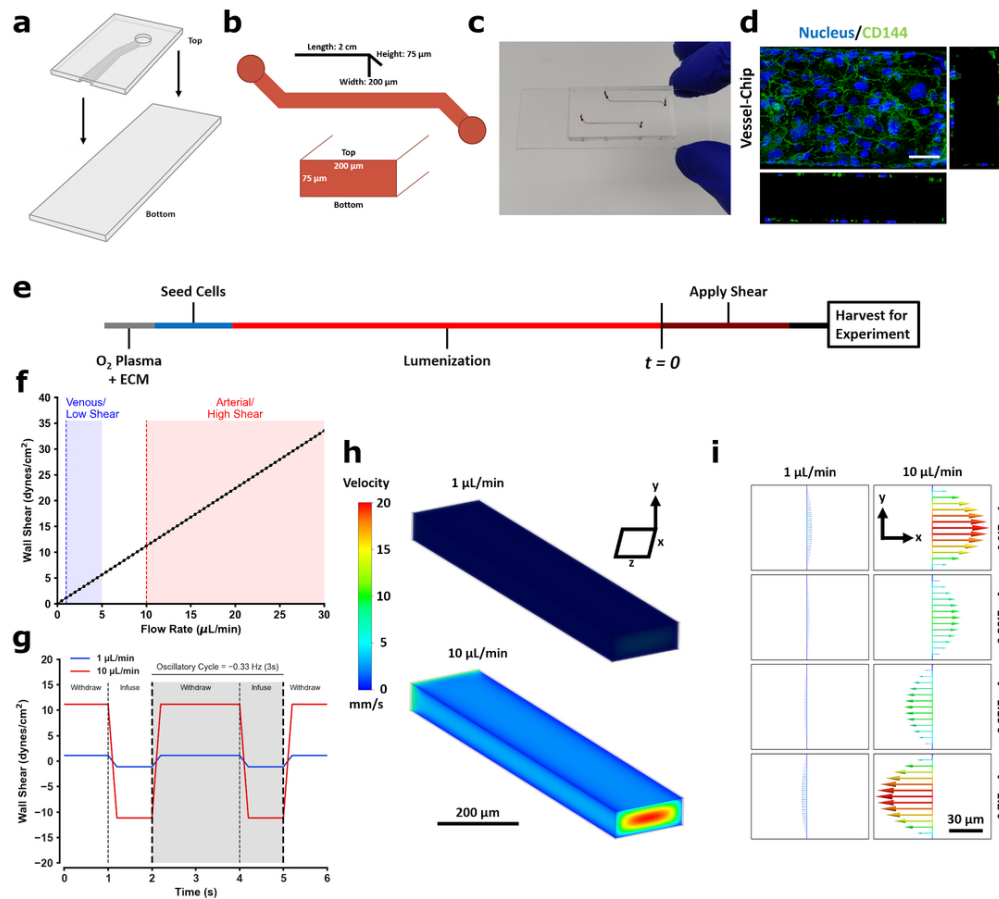
Figure 1: Fabrication of the vessel-chip microfluidic device for endothelial mechanobiology and preliminary quantification. a details the parts of the device bonded together to form a microfluidic channel. The PDMS upper is fabricated via soft-lithography from a positive master mold. The bottom is a glass slide which is left untreated (stiff control) or spin-coated with PDMS to make a fully coated device. The upper and the lower parts are both O2 plasma treated and then bonded together and placed under weight (500 g or greater) for 30 minutes. b lays out the dimensions of the channel. Each channel is 2 cm long, has a height of 75 μm, and a width of 200 μm. The PDMS upper comprises the "top" face of the channel, while the bottom glass slide is the "bottom;" these faces are referred to when seeding cells in the device as both faces are seeded prior to experimentation. c are pictures of a fully fabricated device. d is a representative confocal maximum Z-image of a HUVEC lumen formed on the device using this protocol (Flow Rate: 10 μL/min). e is a graphical schematic of the cell culture protocol used for each experiment. After bonding, devices are O2 plasma treated again and perfused with an ECM matrix (100 μg/mL collagen type I + 50 μg/mL fibronectin) and incubated at 37oC, 5% CO2 for 30 minutes in a cell culture incubator. After the incubation was done, endothelial media (EGM-2) was perfused through the channel to remove excess matrix protein. HUVECs were then seeded on each face. To seed a face, cells were suspended in media and perfused through the channel. The channel was then placed in an incubator for 1 hour to let the cells attach, either right side up to seed the bottom face, or upside down to seed the top face (2 hours total seeding time). After seeding and cell attachment was complete, the channels were placed under perfusion (1 μL/min) for 18 hours to allow for cell proliferation and lumen formation (lumenization). After the 18-hour lumenization was complete, different shear stresses and patterns were applied for the time required for each experiment. 3-dimensional computation fluid analysis of the applied wall shear stress based on the flow rate with corresponding physiological ranges are shown in f, while g details the oscillatory flow pattern used to induce activation (0.3 Hz cycle, 2 seconds withdraw, 1 second infuse). Flow velocity heatmap profiles are shown in h for the unidirectional regimes and the corresponding flow rate, and i details the velocity profile during an oscillatory

cycle, showing the 1-dimensional change in flow direction and magnitude.
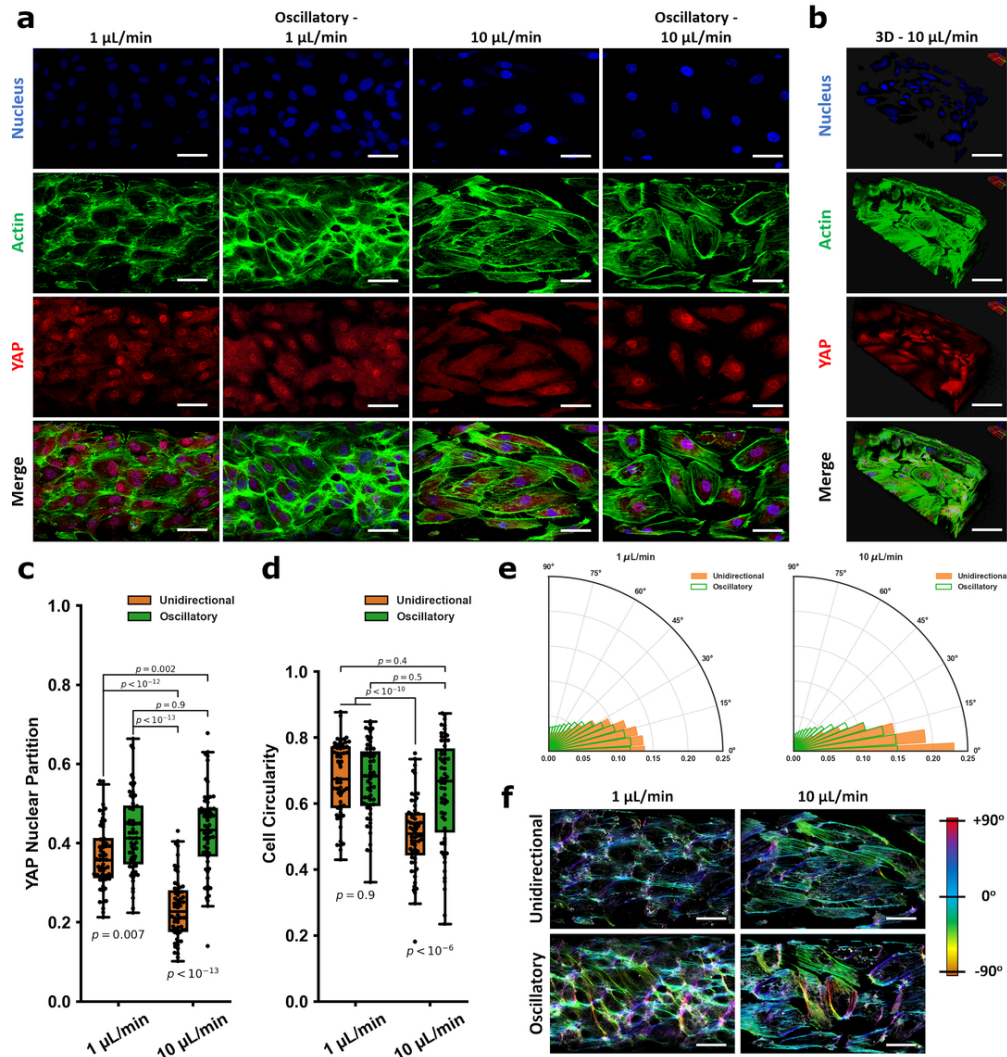
91x82mm (300 x 300 DPI)

Figure 2: YAP mechanobiological model validation of the vessel-chip system for studying endothelial mechanobiology. In a are representative fields of view within the vessel-on-a-chip device for 1 µL/min, oscillatory 1 µL/min, 10 µL/min, and oscillatory 10 µL/min flow. Cells were stained for nuclei (DAPI, blue), actin (phalloidin, green,) and YAP (red). Oscillatory flow was induced by alternating between withdrawal (2 seconds) and infuse (1 second). b is a Z-stack image of a section of a vessel-on-a-chip showing lumen formation (10 µL/min). Scale bars in a and b are all 50 µm. YAP partitions for each group are: 1 µL/min: 0.37 ± 0.08; oscillatory 1 µL/min: 0.42 ± 0.1; 10 µL/min: 0.23 ± 0.08; oscillatory 10 µL/min: 0.43 ± 0.11 (c). The cellular morphology (circularity) is quantified in d. Circularity is defined as $4\pi(area/perimeter2)$ and is valued from 0 to 1. Indices closer to 1 indicate more circular cell morphology, while elongated cells have indices closer to 0. CSI measured for the flow fields are: 1 µL/min: 0.67 ± 0.11; oscillatory 1 µL/min: 0.67 ± 0.11; 10 µL/min: 0.51 ± 0.11; oscillatory 10 µL/min: 0.64 ± 0.16. Directionality assays based on actin alignment detailing how HUVECs align along the flow vector within the fluidic chamber under the different shear regimens/patterns are shown in e. Data is visualized in the form of (r,θ) – r is the normalized density of actin filaments aligned at each angle, θ. Higher values of r for a given θ indicate increasing alignment. For 10 µL/min, HUVECs aligned strongly along the flow vector, while the effect was evident but not as strong in the 1 µL/min regime. HUVECs in both oscillatory flow fields showed a markedly decreased alignment distribution around the flow vector. Color maps showing the gradient of actin alignment (from the representative actin images in a) are visualized in f using OrientationJ. For YAP partition experiments and

CSI experiments, n=60 cells. Alignment polar histogram plots are comprised of an average of 5-6 fields of view, directionality calculated from 0o to 90o binned 15 times in ImageJ. Statistics performed using a single factor ANOVA with post-hoc Tukey's test for significance. Each p-value between groups is reported natively as calculated, significance taken at $p < 0.05$. All values reported as mean ± standard deviation.
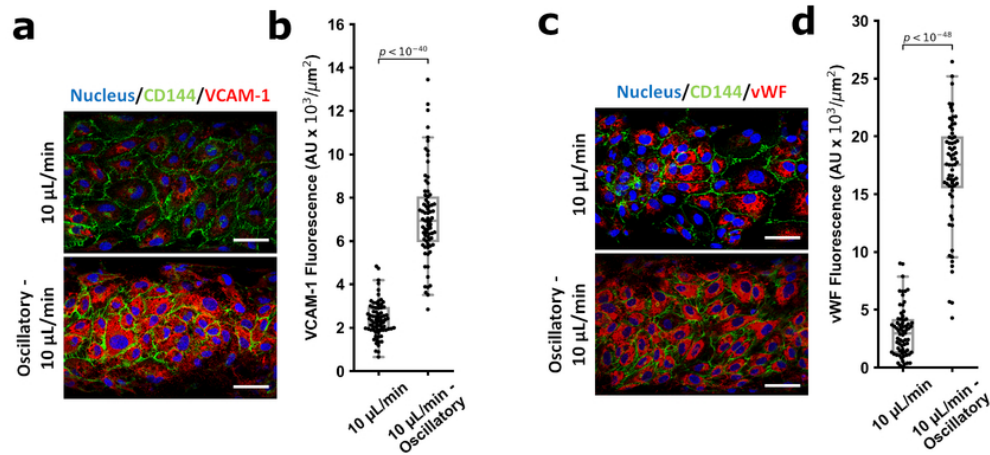
91x99mm (300 x 300 DPI)

Figure 3: Endothelial activation studies between the different shear regimes. In order to establish the system parameters causing activation of YAP correlate to endothelial activation, 2 markers of endothelial inflammation (VCAM-1 and vWF) were examined under the laminar and oscillatory flow conditions. For both markers, oscillatory flow patterns resulted in marked intensity increases for VCAM-1 (a-b, Fluorescence: 10 µL/min – 2.4 ± 0.8 AUx103/µm2, Oscillatory 10 µL/min – 7.1 ± 2 AUx103/µm2) and vWF (c-d, Fluorescence: 10 µL/min – 3.1 ± 2 AUx103/µm2, Oscillatory 10 µL/min – 17 ± 5 AUx103/µm2). For VCAM-1, n=74 cells; for vWF, n=69 cells. Statistical analysis was performed using an unpaired Student's t-test, significance taken at $p < 0.05$. Data is reported as the normalized intensity (to cellular area), mean ± standard deviation.
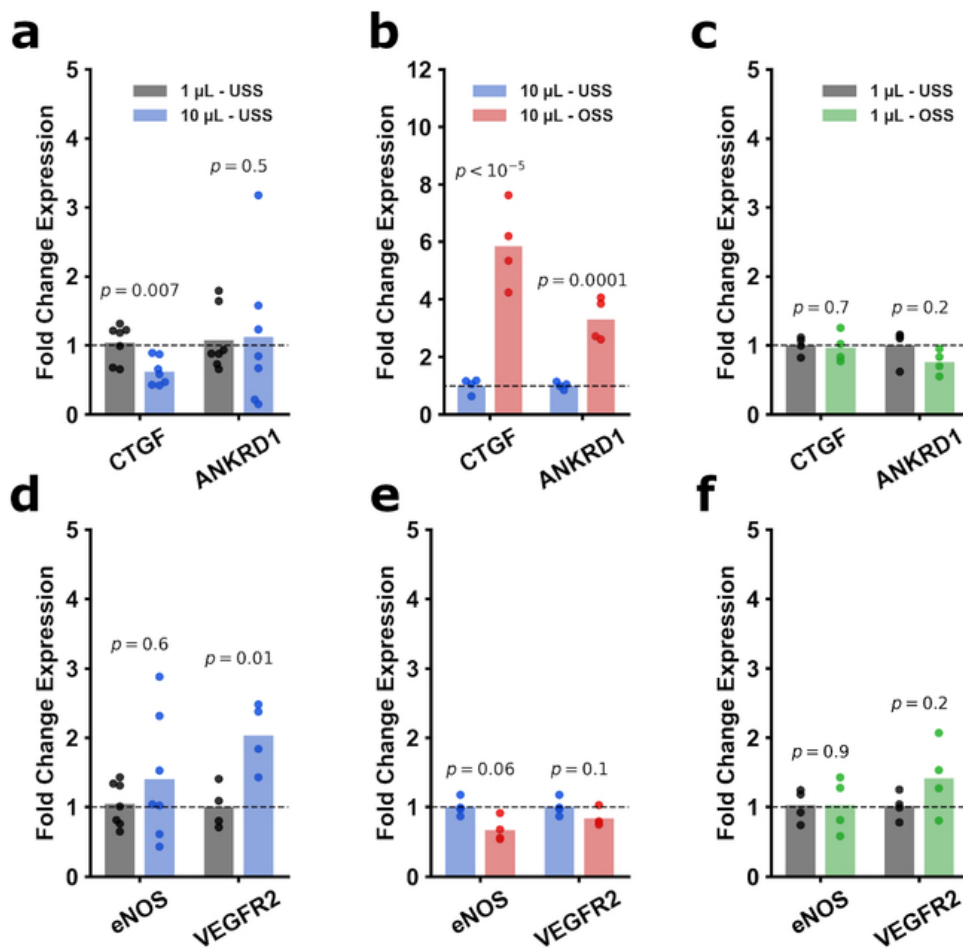
71x33mm (300 x 300 DPI)

Figure 4: Gene expression for key mechanosensitive genes were selected as transcriptional readouts (CTGF, ANKRD1, eNOS, and VEGFR2). CTGF expression was significantly decreased from 1 µL/min to 10 µL/min (a, FC = 0.6) while ANKRD1 was not changed (FC = 1.1). However, oscillatory 10 µL/min vs. 10 µL/min displayed a marked upregulation of both CTGF and ANKRD1 (b, respectively FC = 5.9 and FC = 3.3). Conversely, expression of CTGF and ANKRD1 in the oscillatory 1 µL/min vs. 1 µL/min regime was not changed (b, FC = 0.97 and FC = 0.76). With regards to eNOS and VEGFR2, from 1 µL/min to 10 µL/min, eNOS was not appreciably changed, though VEGFR2 saw modest upregulation (d, FC = 1.4 and FC = 2.0, respectively). Oscillatory 10 µL/min vs. 10 µL/min shown downward trends for both genes (e, FC = 0.67 and FC = 0.83) without reaching significance. Oscillatory 1 µL/min compared to 1 µL/min showed (f, FC = 1.0 and FC = 1.4). Verteporfin immunofluorescence (for nuclei (DAPI, blue), actin (phalloidin, green,) and YAP (red), k) showed decreasing YAP nuclear partitioning in the 1 µM groups vs. DMSO controls (DMSO: 0.46 ± 0.1; 1 µM: 0.30 ± 0.1, l). Gene expression analysis of CTGF and ANKRD1 post-verteporfin treatment (m) showed significant downregulation of CTGF (FC = 0.11) and insignificant modulation of ANKRD1 (FC = 0.70). For a and d CTGF, ANKRD1, and eNOS, n=7; all other genes performed n=4. Statistical analysis was performed on the ddCts for each group using an unpaired Student's t-test. All p-values are reported natively, significance taken at p < 0.05. Values are reported as FC. GAPDH was selected as the housekeeping gene for all experiments.
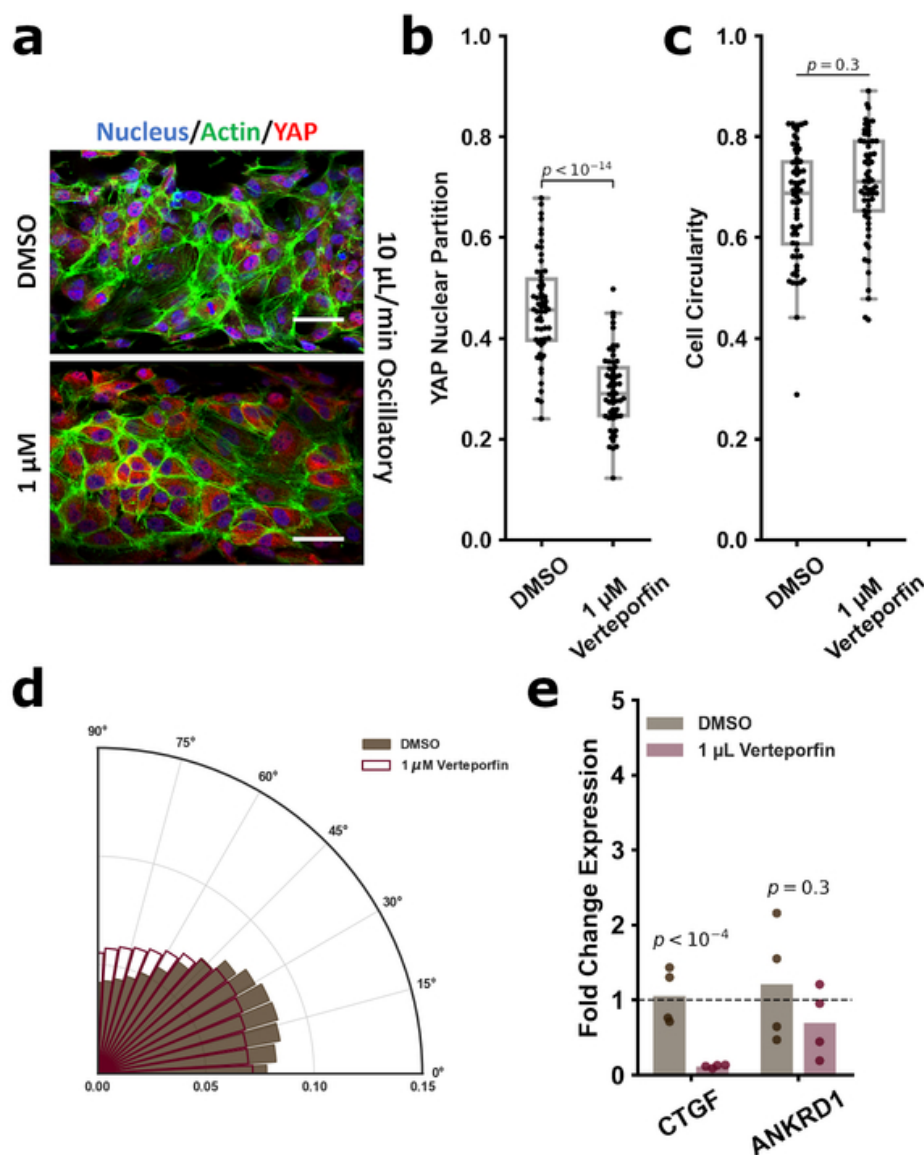
56x54mm (300 x 300 DPI)

Figure 5: Verteporfin immunofluorescence (for nuclei (DAPI, blue), actin (phalloidin, green,) and YAP (red), a) showed decreasing YAP nuclear partitioning in the 1 µM group vs. DMSO control (DMSO: 0.46 ± 0.1; 1 µM: 0.30 ± 0.1, b). Verteporfin treatment did not rescue cellular morphology or alignment under oscillatory flow (c-d). Cell circularity indices for the DMSO and 1 µM Verteporfin groups were respectively 0.67 ± 0.1 and 0.71 ± 0.1. Gene expression analysis of CTGF and ANKRD1 post-verteporfin treatment (e) showed significant downregulation of CTGF (FC = 0.11) and insignificant modulation of ANKRD1 (FC = 0.70). Verteporfin treatment IF and circularity performed on n>59 cells. YAP partition is defined as (nuclear YAP/total YAP). Circularity is defined as $4\pi(area/perimeter2)$ and is valued from 0 to 1. Alignment polar histogram plots are comprised of an average of 4-5 fields of view, directionality calculated from 0o to 90o binned 15 times in ImageJ. Data is visualized in the form of (r,θ). Higher values of r for a given θ indicate increasing alignment in that direction. Gene expression performed n=4. Statistical analysis was performed on the calculated normalized IF values or ddCts for each group using an unpaired Student's t-test. All p-values are reported natively, significance taken at $p < 0.05$. Values are reported as circularity, FC, or normalized intensity, mean ± standard deviation. GAPDH was selected as the housekeeping gene for all

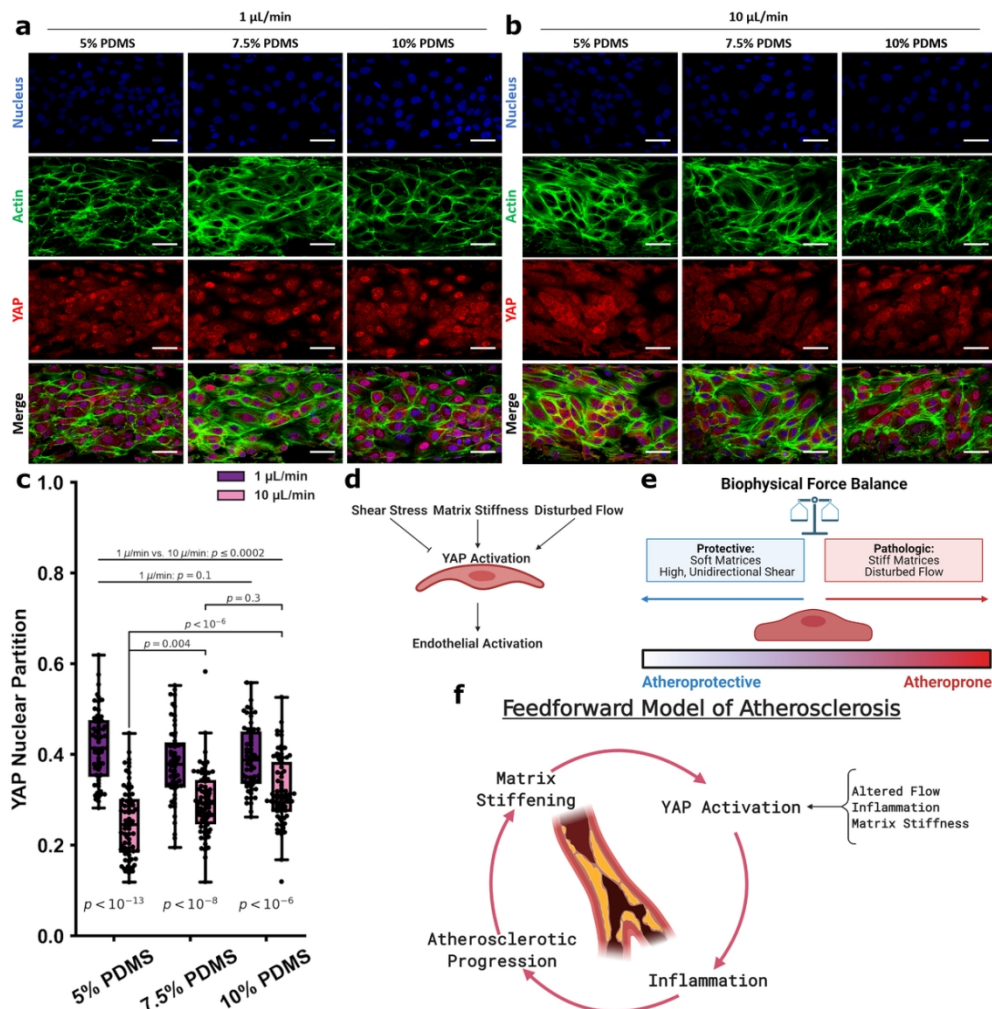experiments.

51x62mm (300 x 300 DPI)

Figure 6: Varying device stiffness to modulate the HUVEC endothelial mechanoresponse. Experiments were performed in devices made form the varied crosslinker concentrations of 5%, 7.5%, and 10% and under the unidirectional shear regimes of 1 µL/min and 10 µL/min. Cells were stained for nuclei (DAPI, blue), actin (phalloidin, green,) and YAP (red), shown in a-b. Across the 1 µL/min groups, YAP partitioning was not affected by substrate stiffness (5%: 0.42 ± 0.1; 7.5%: 0.38 ± 0.1; 10%: 0.39 ± 0.1), while those subject to 10 µL/min showed increasing YAP partition as the substrate stiffened (5%: 0.25 ± 0.1; 7.5%: 0.29 ± 0.1; 10%: 0.32 ± 0.1, c). YAP nuclear partitioning between the 1 µL/min and 10 µL/min groups were significantly different between any 2 groups from different shear regimes. This suggests that ECs respond to a variety of mechanical cues which can either be protective or inflammatory (d-e). The physical regimes of stiffness and shear stress may be connected via YAP mechanobiology in a feedforward manner where an initial incident can result in propagating stiffening and YAP activity (f). For the 1 µL/min groups, n = 56 cells, for the 10 µL/min groups, n = 71-73 cells). Statistics performed using a single factor ANOVA with post-hoc Tukey's test for significance. Each p-value between groups is reported natively as calculated, significance taken at p < 0.05. All values reported as mean ± standard deviation.

105x106mm (300 x 300 DPI)